Phase transformations and phase segregation during potassiation of SnxPy anodes

Ells, Andrew W.; Evans, Matthew L.; Groh, Matthias F.; Morris, Andrew; Marbella, Lauren E.

DOI:
10.1021/acs.chemmater.2c01570

CHEMISTRY OF MATERIALS

pubs.acs.org/cm

Article

Phase Transformations and Phase Segregation during Potassiation of Sn_xP_y Anodes

Andrew W. Ells, Matthew L. Evans, Matthias F. Groh, Andrew J. Morris,* and Lauren E. Marbella*

Cite This: https://doi.org/10.1021/acs.chemmater.2c01570

Read Online

ACCESS | Metrics & More | Article Recommendations | Supporting Information

ABSTRACT: K-ion batteries (KIBs) have the potential to offer a cheaper alternative to Li-ion batteries (LIBs) using widely abundant materials. Conversion/alloying anodes have high theoretical capacities in KIBs, but it is believed that electrode damage from volume expansion and phase segregation by the accommodation of large K-ions leads to capacity loss during electrochemical cycling. To date, the exact phase transformations that occur during potassiation and depotassiation of conversion/alloying anodes are relatively unexplored. In this work, we synthesize two distinct compositions of tin phosphides, Sn_4P_3 and SnP_3, and compare their conversion/alloying mechanisms with solid-state nuclear magnetic resonance (SSNMR) spectroscopy, powder X-ray diffraction (XRD), and density functional theory (DFT) calculations. *Ex situ* ^{31}P and ^{119}Sn SSNMR analyses reveal that while both Sn_4P_3 and SnP_3 exhibit phase separation of elemental P and the formation of KSnP-type environments (which are predicted to be stable based on DFT calculations) during potassiation, only Sn_4P_3 produces metallic Sn as a byproduct. In both anode materials, K reacts with elemental P to form K-rich compounds containing isolated P sites that resemble K_3P but K does not alloy with Sn during potassiation of Sn_4P_3. During charge, K is only fully removed from the K_3P-type structures, suggesting that the formation of ternary regions in the anode and phase separation contribute to capacity loss upon reaction of K with tin phosphides.

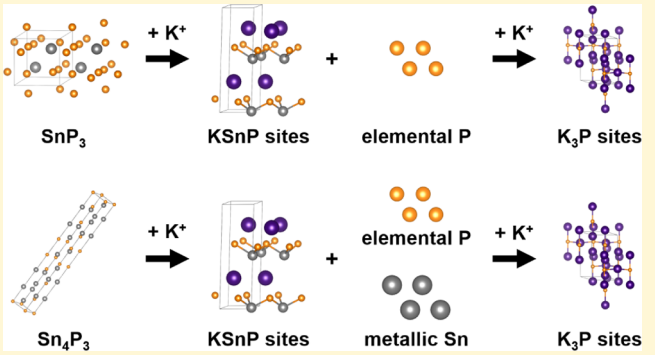

INTRODUCTION

Conversion- and alloying-type anodes offer high capacities in alkali metal batteries, such as commercially successful Si anodes in Li-ion batteries (LIBs). Due to the greater abundance of K compared to Li (and the ability to use aluminum current collectors), K-ion batteries (KIBs) have the potential to lower the cost of grid-scale electrochemical storage[1−3] and reduce demand pressure on Li. However, KIBs are still a nascent technology compared to LIBs, requiring new avenues of electrode and electrolyte materials design.[4−7] K-ion conversion electrodes that can accommodate the large volume changes associated with K insertion/removal while simultaneously delivering practical energy densities are being actively developed. Phosphorus- and phosphide-based compounds display high theoretical specific capacity for KIBs,[8−12] making these materials attractive to study as potential anodes. In particular, binary metal phosphides provide a route to mitigate the large volume expansion observed upon conversion reactions with phosphorus (up to 600% for the formation of K_3P) by producing ternary intermediates and/or displacement and subsequent conversion reactions during potassiation of the parent phase.[13−18]

Of the binary compounds, tin phosphides are readily synthesized in a variety of different stoichiometries (e.g., Sn_4P_3, SnP, Sn_3P_4, and SnP_3[19,20]) offering a rich phase space to study the mechanisms underpinning potassiation/depotassiation in high-capacity (>600 mAh g^{-1}) anodes. Yet, many of the intermediates generated upon K reaction with tin phosphides are highly disordered and separate into multiple phases, making structural assignment challenging. For example, Guo and co-workers used *operando* X-ray diffraction (XRD) to examine the potassiation behavior in Sn_4P_3, proposing a mechanism by which the Sn_4P_3 phase-separates into metallic Sn and amorphous P upon discharge to ∼0.21 V vs K^+/K, allowing the formation of K_3P_{11}.[21] After further discharge to potentials below 0.17 V vs K^+/K, K_3P_{11} reacts with additional K to form K_3P and metallic Sn alloys with K to form KSn. However, each of these assignments relied on a singular, low-intensity reflection in the XRD pattern (12.71° (for KSn), 12.14° (for K_3P_{11}), and 14.27° (for K_3P)). Li and co-workers also report segregation of Sn_4P_3 and Sn, followed by conversion and alloying reactions that form K_3P, KSn, and

Received: May 25, 2022
Revised: July 18, 2022

K_4Sn_{23}, although these assignments rely on minor, low-intensity XRD reflections or lattice spacing measurements from high-resolution transmission electron microscopy (HRTEM) of the crystalline components.[22] In another study, Park and co-workers reported on the final discharge products formed at the end of potassiation of SnP_3 using *ex situ* XRD, HRTEM, and X-ray photoelectron spectroscopy (XPS).[23] The authors proposed a reaction pathway that included phase separation of Sn particles from bulk SnP_3 and a conversion reaction between the remaining P and K to form K_3P. The Sn followed a two-step alloying reaction to first form K_4Sn_{23} and then KSn. Yet only one reflection could be observed for each intermediate in the diffraction data, indicating that heterogeneity and disorder in the anode complicate structural analyses.

Experimental and computational tools that can identify and parse amorphous, multicomponent species with high chemical resolution are required to understand and control complex potassiation behavior in binary anodes. In this study, we use a combination of ^{31}P and ^{119}Sn solid-state nuclear magnetic resonance (SSNMR) spectroscopy and density functional theory (DFT) calculations of stability and simulated NMR spectra for a large set of hypothetical structures to elucidate the amorphous and short-range crystalline structure in products that form during potassiation/depotassiation of SnP_3 and Sn_4P_3. Assignments of crystalline structures are supported via *ex situ* XRD at different states of discharge/charge of KIBs assembled with both anode materials. Both experiment and theory suggest that SnP_3 and Sn_4P_3 exhibit distinct potassiation mechanisms. K insertion into Sn_4P_3 and SnP_3 generates local environments resembling K-Sn-P ternary phases that are predicted to be stable based on DFT calculations. Displacement of metallic Sn is observed in the case of Sn_4P_3, but no Sn phase separates upon potassiation of SnP_3. Unambiguous assignment of metallic Sn during K insertion is achieved by monitoring the metallic Knight shift in ^{119}Sn NMR (metals give rise to unique NMR shifts that are well resolved from diamagnetic compounds due to coupling between nuclei and conduction electrons[24]). When metallic Sn is present, little to no K−Sn alloying is observed.

EXPERIMENTAL SECTION

Materials and Methods. Potassium metal (chunks in mineral oil, 98% trace metals basis), potassium hexafluorophosphate (KPF_6, > 99.5%), propylene carbonate (PC, anhydrous, > 99%), dimethyl carbonate (DMC, anhydrous, > 99%), hexanes (anhydrous, > 99%), Sn (> 99%), and sodium carboxymethyl cellulose (CMC) were purchased from Sigma-Aldrich. Red phosphorous powder (98.9%) was purchased from Alfa Aesar. Carbon Super P was purchased from MTI Corporation. Prior to use, KPF_6 salt was dried *in vacuo* overnight at 100 °C before bringing into an Ar-filled glovebox (O_2 < 0.1 ppm, H_2O < 0.5 ppm). All other materials were used as received.

Synthesis of SnP_3 and Sn_4P_3. SnP_3 and Sn_4P_3 were prepared by first mixing Sn and red P in 1:3 and 4:3 molar ratios, respectively, in a stainless-steel ball mill in an Ar-filled glovebox. Powder mixtures were ball-milled in a SPEX 8000M Mixer/Mill for 8 h (SnP_3) and 1 h (Sn_4P_3). Product purity was confirmed with XRD and SSNMR.

Electrode Fabrication. Electrode films were created by mixing an 8:1:1 mass ratio of Sn_xP_y:carbon Super P:CMC binder. First, the Sn_xP_y and carbon Super P were mixed in a stainless-steel ball mill under Ar for 30 min. In a mortar and pestle, water was added dropwise (~10 drops per 100 mg of dry mixture) to CMC binder until a slurry was formed. The Sn_xP_y and carbon mixture was then added and mixed to make a uniform slurry. The slurry was cast onto a Cu current collector (6 μm thick, MTI) using a 150 μm doctor blade and dried at 100 °C under vacuum overnight. The dried film was punched into 12.7 mm diameter disks to use in cell assembly. Typical mass loadings of active material (Sn_xP_y) per anode were 5−15 mg cm^{-2}. To assemble the opposing K electrodes, K metal was first treated by rinsing thoroughly in hexanes, then removing the external oxide layer with a razor blade. Small pieces of potassium were then placed in a bag coated with hexanes and rolled into thin sheets (~0.25 mm thick) using a cylindrical weight. The K sheet was then removed from the bag and, after waiting for the hexanes to evaporate, stamped into 12.7 mm diameter disks. These electrodes were used for all electrochemical testing and NMR characterization.

Electrochemical Cycling. 2032-type coin cell casings were used to assemble K/SnP_3 and K/Sn_4P_3 half-cells with 15 mm diameter glass microfiber separators (purchased from GE Life Sciences) soaked with 0.8 M KPF_6 in PC. Galvanostatic cycling experiments were performed at C/200 and C/100 for SnP_3 and Sn_4P_3, respectively (where *n*C refers to full theoretical discharge in 1/*n* h). C-rates were calculated from the theoretical capacities of SnP_3 and Sn_4P_3 for the formation of K_3P and KSn (1266 and 613 mAh g^{-1}, respectively). Cells were discharged to 0.05 V and charged to 2.00 V vs K^+/K.

Electrode Extraction. Table 1 summarizes the states of charge at which galvanostatic cycling was stopped for electrode extraction and characterization. After cycling, the Sn_xP_y electrode was removed from the coin cell and submerged in DMC for 30 s before drying at room temperature under vacuum for 30 min. Extraction was performed in an Ar-filled glovebox within, at most, 4 h after cells completed cycling. To collect data for the pristine electrodes, Sn_xP_y electrodes were assembled into coin cells, then immediately removed, washed, and dried as described.

Table 1. States of Charge (V vs K^+/K) Where Sn_xP_y Electrodes Were Extracted for Structural Analysis with XRD and NMR

		XRD	NMR
SnP_3	discharge	1.50, 0.67, 0.53, 0.47, 0.35, 0.06	0.53, 0.06
	charge	1.77, 2.00	1.77, 2.00
Sn_4P_3	discharge	0.90, 0.26, 0.21, 0.18, 0.11, 0.06	0.18, 0.06
	charge	1.50, 2.00	1.50, 2.00

X-ray Diffraction. XRD patterns were collected on a PANalytical XPERT3 powder diffractometer with Cu Kα radiation. To confirm synthesis, pristine SnP_3 and Sn_4P_3 powders were removed from the Cu current collector and placed directly on a zero-background Si plate in the glovebox and sealed with Kapton polyimide film (Chemplex) in an air-free sample holder for data collection. To conduct *ex situ* measurements, individual Sn_xP_y electrodes (including the Cu current collector) were placed on a zero-background Si plate and sealed in the same manner. Reference powder diffraction patterns for SnP_3 and Sn_4P_3 are from the Inorganic Crystal Structure Database (Collection Codes 16293 and 15014, respectively). Rietveld refinement was performed using the TOPAS Academic software package (version 7.12). The crystallite sizes were estimated by a Voigt-convolution approach according to Balzar et al., assuming a lognormal size distribution.[25,26]

One-Dimensional (1D) NMR Measurements. SSNMR experiments were performed at room temperature on a Bruker Avance NEO 600 MHz spectrometer equipped with a 1.6 mm HFXY magic-angle spinning (MAS) Phoenix NMR probehead. Sn_xP_y electrodes at various states of charge were washed and dried as described above. The Sn_xP_y active material was then scraped from the Cu current collector, ground in a mortar and pestle, and packed in a 1.6 mm o.d. ZrO_2 rotor in an Ar-filled glovebox. 1D ^{31}P NMR (90° single pulse, 10 s recycle delay, 2048 scans) experiments were referenced to the ^{31}P shift of solid ammonium dihydrogen phosphate at 0.8 ppm. The recycle delay for ^{31}P NMR experiments was optimized on the pure phase binary compounds. ^{119}Sn NMR was collected using a rotor-synchronized Hahn echo (90°−τ−180°−τ−acquire, where τ = 55.6 and 35.7 μs for 18 and 28 kHz MAS frequency, respectively) pulse

https://doi.org/10.1021/acs.chemmater.2c01570
Chem. Mater. XXXX, XXX, XXX−XXX

sequence. ^{119}Sn NMR was collected at two separate offset frequencies: one corresponding to metallic Sn at 6894 ppm with 46,080 scans and 0.5 s recycle delay, and a second corresponding to diamagnetic Sn compounds and alloys at −153 ppm with 512 scans and 60 s recycle delay, unless otherwise noted. ^{119}Sn NMR shifts were externally referenced to SnO_2 at −604.3 ppm.

Density Functional Theory Calculations. The ternary K−Sn−P composition space has been recently explored using various crystal structure prediction techniques, namely, *ab initio* random structure searching (AIRSS), evolutionary algorithms, and structural prototyping,[27,28] yielding a wealth of predicted stable and metastable phases that could form during electrochemical cycling. Gauge Including Projector Augmented Waves (GIPAW) calculations were performed with CASTEP (v20)[29,30] to predict the ^{31}P chemical shifts for these stable and low-lying metastable phases of K−Sn−P reported in previous work.

The GIPAW-NMR calculations employed the PBE functional,[31] Vanderbilt ultrasoft pseudopotentials,[32] and a plane-wave cutoff energy of 650 eV. The Brillouin zone was consistently sampled with Monkhorst−Pack grids of maximum spacing of $2\pi \times 0.02$ Å^{-1}.[33] All structures were relaxed until the forces on each ion fell below 0.01 eV/Å^{-1} prior to performing the chemical shielding calculations; any structures exhibiting metallicity at the PBE level of theory were excluded from the subsequent GIPAW calculations due to the difficulty of reliably simulating chemical shielding of paramagnetic systems.[34] The computed chemical shielding tensors were referenced against reported experimental ^{31}P shifts for black P, LiP_5, Li_3P, NaP, and Na_3P to provide chemical shift tensors (Figure S9), showing good agreement (fit gradient of −0.997, R^2, of 0.996).[35,36] All of the described calculations and analyses were performed at high throughput with the open-source Python library matador.[27]

RESULTS

Synthesis and Characterization of Tin Phosphide Anodes. SnP_3 and Sn_4P_3 were synthesized by ball-milling stoichiometric amounts of Sn and P. The structural integrity of SnP_3 and Sn_4P_3 after ball-milling with conductive carbon for electrode fabrication was confirmed by XRD (Figure 1). Rietveld refinement of XRD patterns from the SnP_3 and Sn_4P_3 films indicates that the average grain sizes of the active materials are 9 and 16 nm, respectively (assuming a lognormal distribution). Nano-sized active materials are consistent with previously reported syntheses for use in KIBs.[23,37] Particles in this size range are expected to improve transport through the active material and may be less prone to fracture and pulverization during electrochemical cycling compared to micron-sized particles.[38]

Electrochemical Characterization of Tin Phosphides and Possible Potassiation Pathways. The experimental galvanostatic discharge/charge plot (Figure 2) shows that tin phosphides exhibit first-cycle discharge capacities of 176 (for SnP_3) and 235 mAh g^{-1} (for Sn_4P_3). The lower discharge capacity compared to the theoretical capacity is consistent with either deviation from the predicted potassiation pathway and/or sluggish kinetics that prevent K insertion in the active material. The shape of the voltage profile observed upon the charge of SnP_3 is similar to the discharge curve, albeit at lower capacity, suggesting that potassiation may be only partially reversible and/or that side reactions occur on the first discharge. In contrast, the voltage profile for K removal from Sn_4P_3 is substantially more sloped, indicating that different phase transformations may occur during depotassiation. Voltage profiles for later cycles retain these features (Figure S1).

To understand the possible phase transformations taking place during potassiation/depotassiation of the tin phosphide

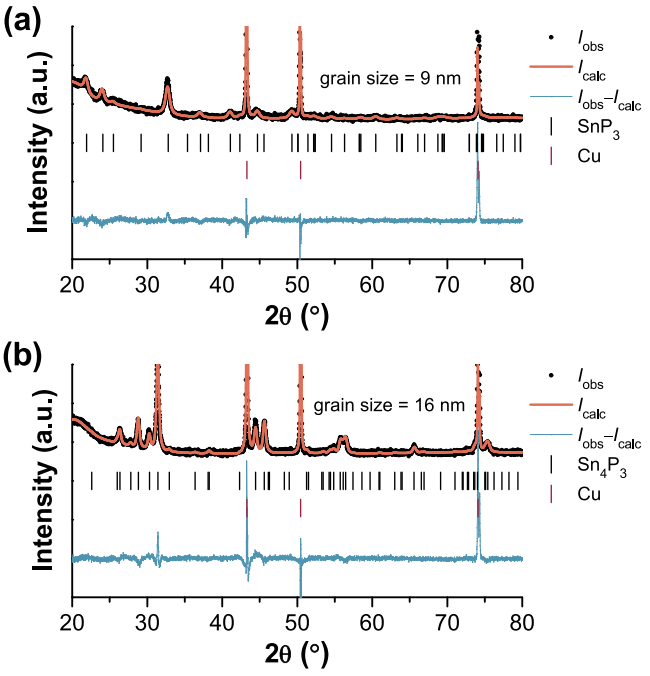

Figure 1. Rietveld refinement of the XRD pattern corresponding to (a) SnP_3 and (b) Sn_4P_3 films after ball-milling with conductive carbon, mixing with CMC, and coating on Cu foil. The crystallite sizes were estimated using a Voigt-convolution approach according to ref 25, assuming a lognormal size distribution.

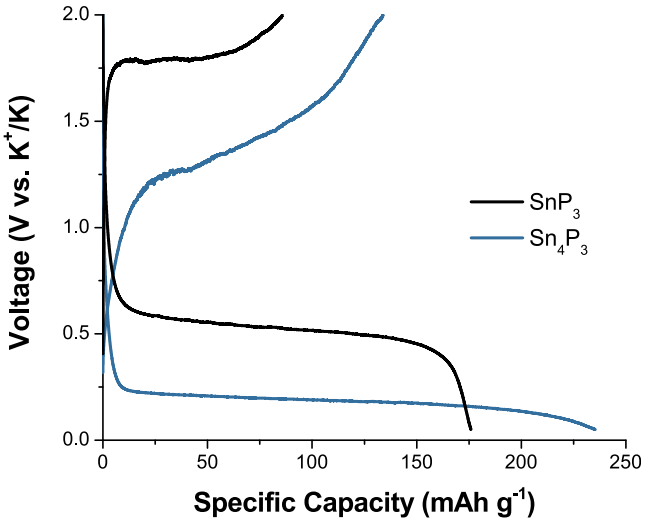

Figure 2. Voltage profiles of first-cycle discharge/charge for SnP_3 (black line) and Sn_4P_3 (blue line) during galvanostatic cycling at C/200 and C/100, respectively.

anodes, we first turn to DFT. DFT calculations describe the thermodynamic stability of several phases in the relevant composition space, many of which are not currently reported in crystal structure databases, computational or otherwise (indicated with an asterisk (*) in the following lists). The full predicted phase space is elaborated elsewhere;[39] in this work, the local environments from low-lying trial structures are used to provide insight into the short-range structural motifs formed during cycling and probed with SSNMR and XRD (vide infra).

No crystal structures for ternary K−Sn−P compounds exist in current databases. Our DFT calculations predict that KSn_2P_2, KSn_3P_3, KSnP, K_5SnP_3, and K_8SnP_4 are all stable

https://doi.org/10.1021/acs.chemmater.2c01570
Chem. Mater. XXXX, XXX, XXX−XXX

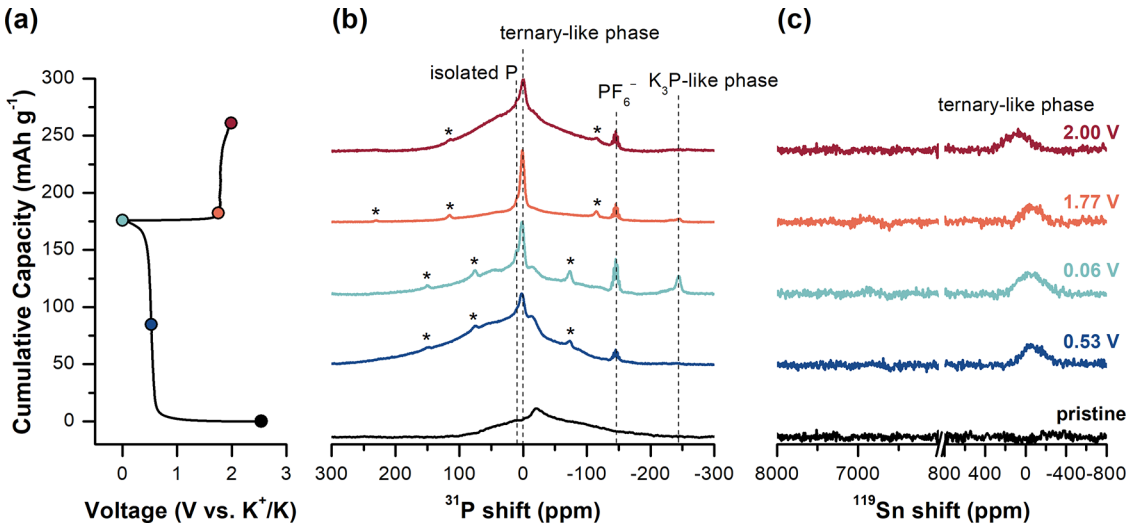

Figure 3. (a) Voltage profile of first discharge/charge of SnP_3 under galvanostatic conditions at C/200. Colored points mark the states of charge at which cycling was stopped and SnP_3 anodes were extracted for structural analysis. *Ex situ* (b) ^{31}P and (c) ^{119}Sn SSNMR of SnP_3 anodes during the initial discharge (blue-hue spectra) and charge (red-hue spectra). The ^{31}P quintet at −146 ppm (J_{P-F} = 675 Hz) is assigned to residual PF_6^- from the electrolyte. Asterisks indicate spinning sidebands. Experiments were performed at either 18 or 28 kHz MAS frequency.

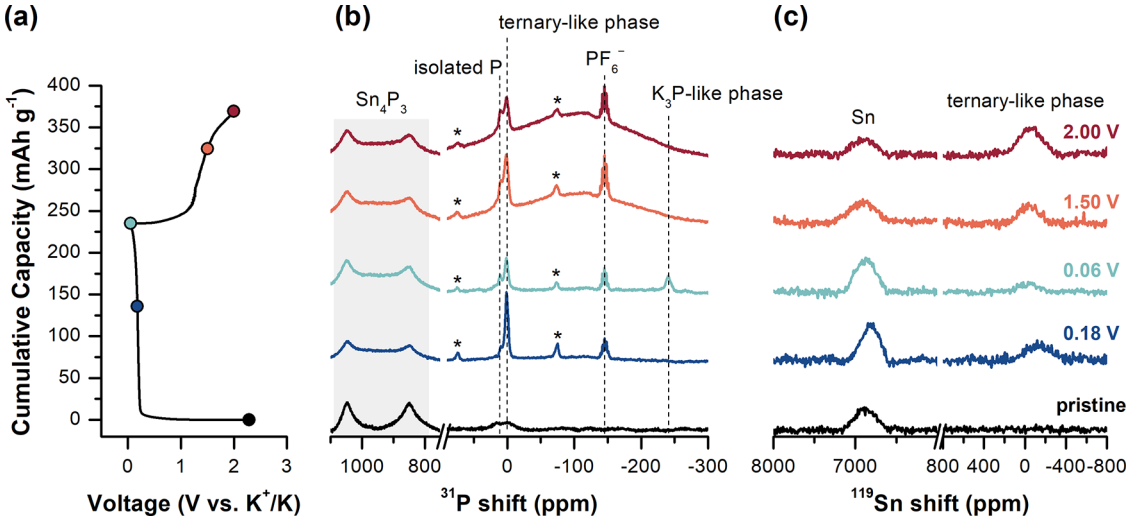

Figure 4. (a) Voltage profile of first discharge/charge of Sn_4P_3 under galvanostatic conditions at C/100. Colored points mark the states of charge at which cycling was stopped and Sn_4P_3 anodes were extracted for structural analysis. *Ex situ* (b) ^{31}P and (c) ^{119}Sn SSNMR of Sn_4P_3 anodes during the initial discharge (blue-hue spectra) and charge (red-hue spectra). The ^{31}P quintet at −146 ppm (J_{P-F} = 675 Hz) is assigned to residual PF_6^- from the electrolyte. All experiments were performed at 18 kHz MAS frequency.

phases that may be formed during potassiation or depotassiation of either Sn_4P_3 or SnP_3 anodes (shown in Figure S2). For the K−P edge, each of KP_{15}, KP_7*, K_3P_{11}, K_3P_7*, K_2P_3, KP, and K_5P_4* are predicted to be stable. Most notably, calculations performed with the PBE functional also indicate that two possible charging endpoints, K_4P_3 and K_3P, are both only metastable at finite temperatures; however, they both lie very close to the convex hull (+2 and +5 meV/atom, respectively). Applying instead the rSCAN functional,[40,41] K_3P is found to be thermodynamically stable, yet lies almost precisely on the existing tie-line between K_5P_4 and K, indicating that this phase may not form unless cycled to very low voltages (0.01 V vs K^+/K). Similar calculations for the K−Sn phase space indicate that there are three stable K−Sn phases, namely, K_3Sn_{17} (which destabilizes the known K_4Sn_{23} phase), K_4Sn_9, and KSn.

We note that while DFT-predicted thermodynamic stability is useful for screening individual trial structures, the formation of a given phase during electrochemical cycling is highly dependent on kinetics.

Experimental Characterization of Potassiation/Depotassiation Mechanisms of SnP_3 and Sn_4P_3. *Ex situ* ^{31}P and ^{119}Sn SSNMR were collected at multiple states of charge to directly measure the local structural environments present in tin phosphide anodes during potassiation/depotassiation (Figures 3 and 4). Pristine SnP_3 (Figure 3, black) exhibits a broad ^{31}P signal ranging from 100 to −210 ppm, in addition to a sharp (fwhm ∼12 ppm) resonance centered at −20 ppm. Since $R\bar{3}m$-SnP_3 only contains one independent P site, the combination of broad and sharp lines for pristine SnP_3 likely arises from small particle sizes (∼9 nm) observed in XRD after prolonged ball milling during synthesis (8 h) and/or amorphous SnP_3 compounds. For nano-sized materials, atoms

https://doi.org/10.1021/acs.chemmater.2c01570
Chem. Mater. XXXX, XXX, XXX−XXX

in the particle core often display a sharp resonance consistent with the bulk crystalline material, whereas the surface sites exhibit inhomogeneous broadening.[42−44] In the pristine state, ^{119}Sn SSNMR does not show a resonance for SnP_3 (Figure 3c, black), possibly due to long spin-lattice (T_1) relaxation times, in combination with inhomogeneous line broadening, making detection prohibitively long[45] (the maximum recycle delay tested in these experiments was 1000 s, and no signal was observed after a frequency sweep from 6400 to −9300 ppm).

After discharge of SnP_3 to the center of the voltage plateau at 0.53 V vs K^+/K (Figure 3, dark blue), a narrow ^{31}P resonance at 2.6 ppm (fwhm ∼23 ppm) appears with a small shoulder at 11 ppm (these peaks are more clearly observed in Figure S6, which depicts the ^{31}P spectra alone). The resonance at 11 ppm is consistent with elemental black P,[46] whereas the peak at 2.6 ppm agrees with the ^{31}P shift predicted for the on-hull $P6_3mc$-KSnP ternary phase discovered with DFT (δ_{iso} = 2.3 ppm, Figure S10). Likewise, a broad ^{119}Sn resonance at −66 ppm (fwhm ∼240 ppm) appears at the same voltage, supporting the formation of new Sn environments that may resemble KSnP-type sites. (N.B. Alkali metal insertion into Sn_xP_y likely decreases T_1 relaxation times,[47−49] allowing us to observe ^{119}Sn resonances during potassiation). The lack of new Bragg reflections in XRD (Figure S3) indicates that crystalline KSnP does not form, but rather that K reaction with SnP_3 results in local environments similar to those found in the ternary KSnP phase (where P is coordinated to three Sn and three K atoms and exhibits C_{3v} symmetry).

In the fully discharged state at 0.06 V vs K^+/K (Figure 3, light blue), we continue to observe the ^{31}P peak corresponding to black P, as well as a new peak at −244.5 ppm; no change is observed in ^{119}Sn NMR. The ^{31}P resonance at −244.5 ppm is similar to that observed for both Na_3P (δ_{iso} = −207 ppm)[46] and Li_3P (δ_{iso} = −275 ppm).[50,51] Examination of the chemical shift anisotropy (CSA) associated with the ^{31}P resonance at −244.5 ppm shows that there is very little anisotropy at this site, consistent with the formation of isolated P atoms, likely surrounded by K, similar to those expected for K_3P (Figure S7, experimental: Δ = 61 ppm, η = 0.07; calculated: Δ = 56 ppm, η = 0.42). These data indicate that phase separation of elemental P enables a conversion reaction between P and K that produces K_3P-like structures. Since there are no additional reflections observed in XRD at the end of discharge (Figure S3), we suspect that these K_3P-like environments do not exhibit long-range order. Further, we do not observe metallic Sn at any state of charge (Figure 3c; Figure S8 shows ^{119}Sn NMR of bulk Sn), indicating that only reactions of K with P and Sn_xP_y lead to the observed capacity.

Ex situ ^{31}P and ^{119}Sn NMR of the intermediates formed during potassiation of Sn_4P_3 are shown in Figure 4. The two resonances centered at 1050 and 850 ppm in the ^{31}P SSNMR of the pristine sample (Figure 4b, black) are assigned to the two independent P sites (at the 6*c* and 3*a* positions, respectively) in $R\bar{3}m$-Sn_4P_3.[50] Minor resonances in ^{31}P and ^{119}Sn NMR spectra are attributed to residual P (at ∼15 ppm) and Sn (center of mass at ∼6870 ppm) from synthesis. Upon discharge to the middle of the voltage plateau at 0.18 V vs K^+/K (Figure 4, dark blue), ^{31}P resonances at 2.6 and approximately 16 ppm are assigned to KSnP-like sites and phase-separated P, respectively. The presence of KSnP-like sites is again reflected in the ^{119}Sn spectra by the resonance centered at −138 ppm; both ^{31}P and ^{119}Sn NMR spectroscopies are consistent with observations from SnP_3 upon initial potassiation. Analysis of ^{119}Sn NMR shows an increase in the NMR signal intensity for metallic Sn, indicating that Sn particles are produced during potassiation. The presence of metallic Sn is also confirmed with XRD, in which multiple small Sn reflections appear at 0.18 V (Figures S4 and S5). At full discharge to 0.06 V vs K^+/K (Figure 4, light blue), K reacts with elemental P to form disordered K_3P-type structures. During discharge/charge, the ^{119}Sn NMR resonance for metallic Sn does not change in width, nor the center of mass, which strongly suggests that metallic Sn particles do not participate in further reactions. DFT and *ex situ* studies of ^{119}Sn NMR during Li−Sn alloying reveal that isotropic ^{119}Sn shifts are very sensitive to alloying (e.g., LiSn has two resonances at 5969 and 5429 ppm compared to a single resonance at 6915 ppm for pure β-Sn).[52,53] We would expect similar ^{119}Sn NMR spectrum changes if K−Sn alloying were taking place.

Depotassiation Mechanisms of SnP_3 and Sn_4P_3. Upon charge of SnP_3 to 1.77 V vs K^+/K (Figure 3, light red), the ^{31}P resonance corresponding to the sites resembling K_3P decreases considerably, while the relative ratio of elemental phosphorus (at 11 ppm) increases, consistent with K removal. At 2.00 V vs K^+/K (Figure 3, dark red), the ^{31}P NMR spectrum of fully charged SnP_3 resembles that of the pristine material, as indicated by the shoulder at 40 ppm and the broad ^{31}P NMR lineshape, but resonances corresponding to KSnP-type sites remain in both ^{31}P and ^{119}Sn NMR. The center of mass of the KSnP-type environment in the diamagnetic region of ^{119}Sn NMR shifts to higher ppm ($\delta_{2.00\ V} - \delta_{1.77\ V}$ = 150 ppm), likely due to changes in the stoichiometry of $K_xSn_yP_z$, some of which may regenerate SnP_3-like sites. Partial reformation of SnP_3 is also consistent with observations from XRD that show increased intensity for SnP_3 reflections upon charging relative to the fully discharged electrode (Figure S3).

Upon depotassiation of Sn_4P_3 to 1.50 V vs K^+/K (Figure 4, light red), K is readily removed from K_3P-type environments, whereas KSnP-type sites persist, similar to SnP_3. Again, K removal leads to small changes in the peak position of $K_xSn_yP_z$ sites in ^{119}Sn NMR and the emergence of a broad peak extending from 170 to −310 ppm in ^{31}P NMR (center of mass = −110 ppm). DFT simulations predict several $K_xSn_yP_z$ phases with ^{31}P chemical shifts in this range, indicating that both Sn_4P_3 and SnP_3 anodes generate highly disordered $K_xSn_yP_z$ coordination environments, although these sites may overlap with inhomogeneous broadening observed for SnP_3 particles. The chemical shift of metallic Sn in ^{119}Sn NMR remains constant (Figure 4) during charge, providing evidence that phase-segregated Sn does not alloy with K.

DISCUSSION

The combination of SSNMR and DFT provides unique insight into the potassiation/depotassiation behavior of tin phosphide anodes. First, we assign a new ternary KSnP-type environment that forms upon discharge of the battery. The formation of KSnP-like coordination environments in both Sn_4P_3 and SnP_3 is consistent with our predictions from DFT that indicate $P6_3mc$-KSnP is thermodynamically stable upon potassiation of both parent compounds. However, differences in stoichiometry and structure between the two tin phosphides suggest that each has a distinct potassiation mechanism that forms these environments. In Sn_4P_3, the two-dimensional structure allows for topotactic intercalation and coordination of K with the alternating rows of Sn and P along the *c*-axis, forming Sn and P

https://doi.org/10.1021/acs.chemmater.2c01570
Chem. Mater. XXXX, XXX, XXX−XXX

coordination environments similar to those found in the KSnP-like sites in NMR. This process leads to displacement of elemental P and concurrent reduction of Sn, but only P undergoes a conversion reaction upon subsequent potassiation. In contrast, the formation of KSnP-like sites in the three-dimensional SnP_3 structure requires cleavage of P−P bonds during reduction. P−P bond cleavage during K insertion results in the phase separation of P observed in ^{31}P NMR, ultimately producing local ^{31}P sites that can coordinate to three nearby Sn atoms (bond distances of 2.72, 2.97, and 3.77 Å) and K to produce the C_{3v} symmetry about the P atom observed in KSnP. This mechanism resembles that proposed by Nazar and co-workers for Li insertion in MnP_4, where reduction is facilitated by P−P bond breakage rather than redox chemistry associated with the metal center.[16] In both tin phosphides, residual KSnP-like sites are present at full charge. This suggests kinetic or transport limitations on K removal and presents a mechanism of capacity fade by which K is locked in the tin phosphide structure. We note that this degradation is in addition to electrode cracking observed in scanning electron microscopy (SEM) of both tin phosphide anodes (Figure S11).

The second major finding of this work is that metallic Sn is only generated in the case of Sn_4P_3, and not in SnP_3 as previously suggested.[23] While this phase-separated Sn can, in principle, provide capacity in terms of K−Sn alloying (analogous to the behavior observed in tin phosphides for Li- and Na-ion batteries[50,54−58]), no evidence for the electrochemical reaction between K and Sn is seen in ^{119}Sn NMR nor XRD. The lack of capacity from metallic Sn is consistent with a loss of electrical contact upon phase separation.[59] Metallic Sn is never reincorporated in the anode, which is consistent with displacement reactions observed in LIB systems producing electrically isolated metal particles upon conversion and displacement reactions (e.g., InSb,[60] Cu_2Sb,[61] CoP_3[17]). Thus, most of the observed capacity in both Sn_4P_3 and SnP_3 is due to the formation of disordered sites resembling K_3P and likely explains the rapid capacity loss in these systems. Efforts to enable alloying anodes in KIBs must consider this phase separation and find a way to tether the components to the electrode during potassiation/depotassiation.

CONCLUSIONS

The combination of SSNMR and DFT enabled the detection and assignment of short-range and amorphous intermediates previously invisible in diffraction analyses of tin phosphide anodes for KIBs. While the intention of binary phosphide anodes, such as tin phosphides, is to enable high capacity and mitigate volume expansion, we find that upon phase separation of elemental P (in both Sn_4P_3 and SnP_3) and metallic Sn (in the case of Sn_4P_3), only P-containing compounds react reversibly with K. Local structures resembling KSnP persist after charge, suggesting transport and/or kinetic limitations for removing K from within the layered tin phosphides (regardless of starting stoichiometry). In the case of Sn_4P_3, the formation of electrically isolated Sn prevents total recovery of the pristine material and does not appear to add reversible capacity via alloying. The irreversible phase separation and structural rearrangements inherent to tin phosphides motivate new approaches to enabling P or binary phosphides as a high-capacity KIB anode material. We suspect that tin phosphides in KIBs may benefit from the approaches taken for Si−C anodes in LIBs,[62−64] where nanoparticles of the high-capacity anode material (for KIBs, P) are embedded in a graphitic matrix to accommodate volume expansion.

ASSOCIATED CONTENT

Supporting Information

The Supporting Information is available free of charge at https://pubs.acs.org/doi/10.1021/acs.chemmater.2c01570.

Additional electrochemistry, structural models, XRD, solid-state NMR spectroscopy, simulated data, and scanning electron microscopy (Figures S1−S11) (PDF)

AUTHOR INFORMATION

Corresponding Authors

Andrew J. Morris − *School of Metallurgy and Materials, University of Birmingham, Birmingham B15 2TT, United Kingdom;* orcid.org/0000-0001-7453-5698; Email: A.J.Morris.1@bham.ac.uk

Lauren E. Marbella − *Department of Chemical Engineering, Columbia University, New York, New York 10027, United States;* orcid.org/0000-0003-1639-3913; Email: lem2221@columbia.edu

Authors

Andrew W. Ells − *Department of Chemical Engineering, Columbia University, New York, New York 10027, United States*

Matthew L. Evans − *Theory of Condensed Matter Group, Cavendish Laboratory, University of Cambridge, Cambridge CB3 0HE, United Kingdom; Institut de la Matière Condensée et des Nanosciences, UCLouvain, Louvain-la-Neuve 1348, Belgium;* orcid.org/0000-0002-1182-9098

Matthias F. Groh − *Institute for Inorganic Chemistry, RWTH Aachen University, Aachen 52074, Germany;* orcid.org/0000-0002-7436-7177

Complete contact information is available at: https://pubs.acs.org/10.1021/acs.chemmater.2c01570

Author Contributions

A.W.E. performed materials synthesis, electrochemistry, XRD characterization, and SSNMR experiments. M.L.E. conducted all DFT simulations and analyses, and contributed to required software. M.F.G. contributed to XRD analysis. A.W.E., M.L.E., L.E.M., and A.J.M. contributed to the conception and design of the study. The manuscript was edited with input from all co-authors. All authors have read and approved the submitted version.

Notes

The authors declare no competing financial interest.

ACKNOWLEDGMENTS

This work was supported by the National Science Foundation (DMR-2116728). A.W.E. was supported by the U.S. Department of Defense through the National Defense Science & Engineering Graduate Fellowship (NDSEG) program. M.L.E. acknowledges the Engineering and Physical Sciences Research Council (EPSRC) Centre for Doctoral Training in Computational Methods for Materials Science, U.K., for funding (EP/L015552/1). M.F.G. is thankful to the support by the Stiftung Stipendien-Fonds des Verbandes der Chemischen Industrie (Liebig grant). A.J.M. acknowledges networking support from

EPSRC's CCP-NC (EP/T026642/1), CCP9 (EP/T026375/1), and UKCP (EP/P022561/1).

REFERENCES

(1) Dhir, S.; Wheeler, S.; Capone, I.; Pasta, M. Outlook on K-Ion Batteries. *Chem* **2020**, *6*, 2442−2460.

(2) Hosaka, T.; Kubota, K.; Hameed, A. S.; Komaba, S. Research Development on K-Ion Batteries. *Chem. Rev.* **2020**, *120*, 6358−6466.

(3) Tian, Y.; Zeng, G.; Rutt, A.; Shi, T.; Kim, H.; Wang, J.; Koettgen, J.; Sun, Y.; Ouyang, B.; Chen, T.; Lun, Z.; Rong, Z.; Persson, K.; Ceder, G. Promises and Challenges of Next-Generation " Beyond Li-Ion" Batteries for Electric Vehicles and Grid Decarbonization. *Chem. Rev.* **2021**, *121*, 1623−1669.

(4) Zhang, W.; Liu, Y.; Guo, Z. Approaching High-Performance Potassium-Ion Batteries via Advanced Design Strategies and Engineering. *Sci. Adv.* **2019**, *5*, No. eaav7412.

(5) Zhou, M.; Bai, P.; Ji, X.; Yang, J.; Wang, C.; Xu, Y. Electrolytes and Interphases in Potassium Ion Batteries. *Adv. Mater.* **2021**, *33*, No. 2003741.

(6) WU, X.; Qiu, S.; Liu, Y.; Xu, Y.; Jian, Z.; Yang, J.; Ji, X.; Liu, J. The Quest for Stable Potassium-Ion Battery Chemistry. *Adv. Mater.* **2022**, *34*, No. 2106876.

(7) Wang, H.; Zhai, D.; Kang, F. Solid Electrolyte Interphase (SEI) in Potassium Ion Batteries. *Energy Environ. Sci.* **2020**, *13*, 4583−4608.

(8) Sultana, I.; Rahman, M. M.; Ramireddy, T.; Chen, Y.; Glushenkov, A. M. High Capacity Potassium-Ion Battery Anodes Based on Black Phosphorus. *J. Mater. Chem. A* **2017**, *5*, 23506−23512.

(9) Huang, X.; Liu, D.; Guo, X.; Sui, X.; Qu, D.; Chen, J. Phosphorus/Carbon Composite Anode for Potassium-Ion Batteries: Insights into High Initial Coulombic Efficiency and Superior Cyclic Performance. *ACS Sustainable Chem. Eng.* **2018**, *6*, 16308−16314.

(10) Xiong, P.; Bai, P.; Tu, S.; Cheng, M.; Zhang, J.; Sun, J.; Xu, Y. Red Phosphorus Nanoparticle@3D Interconnected Carbon Nanosheet Framework Composite for Potassium-Ion Battery Anodes. *Small* **2018**, *14*, No. 1802140.

(11) Wu, Y.; Huang, H. B.; Feng, Y.; Wu, Z. S.; Yu, Y. The Promise and Challenge of Phosphorus-Based Composites as Anode Materials for Potassium-Ion Batteries. *Adv. Mater.* **2019**, *31*, No. 1901414.

(12) Chang, W. C.; Wu, J. H.; Chen, K. T.; Tuan, H. Y. Red Phosphorus Potassium-Ion Battery Anodes. *Adv. Sci.* **2019**, *6*, No. 1801354.

(13) Zhang, W. J. Lithium Insertion/Extraction Mechanism in Alloy Anodes for Lithium-Ion Batteries. *J. Power Sources* **2011**, *196*, 877−885.

(14) Nitta, N.; Yushin, G. High-Capacity Anode Materials for Lithium-Ion Batteries: Choice of Elements and Structures for Active Particles. *Part. Part. Syst. Charact.* **2014**, *31*, 317−336.

(15) Doublet, M. L.; Lemoigno, F.; Gillot, F.; Monconduit, L. The Li_xVPn_4 Ternary Phases (Pn = P, As): Rigid Networks for Lithium Intercalation/Deintercalation. *Chem. Mater.* **2002**, *14*, 4126−4133.

(16) Souza, D. C. S.; Pralong, V.; Jacobson, A. J.; Nazar, L. F. A Reversible Solid-State Crystalline Transformation in a Metal Phosphide Induced by Redox Chemistry. *Science* **2002**, *296*, 2012−2015.

(17) Pralong, V.; Souza, D. C. S.; Leung, K. T.; Nazar, L. F. Reversible Lithium Uptake by CoP_3 at Low Potential: Role of the Anion. *Electrochem. Commun.* **2002**, *4*, 516−520.

(18) Silva, D. C. C.; Crosnier, O.; Ouvrard, G.; Greedan, J.; Safa-Sefat, A.; Nazar, L. F. Reversible Lithium Uptake by FeP_2. *Electrochem. Solid-State Lett.* **2003**, *6*, A162−A166.

(19) Zavrazhnov, A. Y.; Semenova, G. V.; Proskurina, E. Y.; Sushkova, T. P. Phase Diagram of the Sn−P System. *J. Therm. Anal. Calorim.* **2018**, *134*, 475−481.

(20) Gullman, J. The Crystal Structure of SnP. *Journal of Solid State Chemistry* **1990**, *87*, 202−207.

(21) Zhang, W.; Pang, W. K.; Sencadas, V.; Guo, Z. Understanding High-Energy-Density Sn_4P_3 Anodes for Potassium-Ion Batteries. *Joule* **2018**, *2*, 1534−1547.

(22) Li, D.; Zhang, Y.; Sun, Q.; Zhang, S.; Wang, Z.; Liang, Z.; Si, P.; Ci, L. Hierarchically Porous Carbon Supported Sn_4P_3 as a Superior Anode Material for Potassium-Ion Batteries. *Energy Storage Mater.* **2019**, *23*, 367−374.

(23) Verma, R.; Didwal, P. N.; Ki, H. S.; Cao, G.; Park, C. J. SnP_3/Carbon Nanocomposite as an Anode Material for Potassium-Ion Batteries. *ACS Appl. Mater. Interfaces* **2019**, *11*, 26976−26984.

(24) Knight, W. D. Nuclear Magnetic Resonance Shift in Metals. *Phys. Rev.* **1949**, *76*, 1259−1260.

(25) Balzar, D.; Audebrand, N.; Daymond, M. R.; Fitch, A.; Hewat, A.; Langford, J. I.; Le Bail, A.; Louër, D.; Masson, O.; McCowan, C. N.; Popa, N. C.; Stephens, P. W.; Toby, B. H. Size-Strain Line-Broadening Analysis of the Ceria Round-Robin Sample. *J. Appl. Crystallogr.* **2004**, *37*, 911−924.

(26) Coelho, A. A. TOPAS and TOPAS-Academic: An Optimization Program Integrating Computer Algebra and Crystallographic Objects Written in C++: An. *J. Appl. Crystallogr.* **2018**, *51*, 210−218.

(27) Evans, M. L.; Morris, A. J. Matador: A Python Library for Analysing, Curating and Performing High-Throughput Density-Functional Theory Calculations. *J. Open Source Software* **2020**, *5*, 2563.

(28) Harper, A. F.; Evans, M. L.; Darby, J. P.; Karasulu, B.; Koçer, C. P.; Nelson, J. R.; Morris, A. J. Ab Initio Structure Prediction Methods for Battery Materials a Review of Recent Computational Efforts to Predict the Atomic Level Structure and Bonding in Materials for Rechargeable Batteries. *Johnson Matthey Technol. Rev.* **2020**, *64*, 103−118.

(29) Pickard, C. J.; Mauri, F. All-Electron Magnetic Response with Pseudopotentials: NMR Chemical Shifts. *Phys. Rev. B* **2001**, *63*, No. 245101.

(30) Clark, S. J.; Segall, M. D.; Pickard, C. J.; Hasnip, P. J.; Probert, M. I. J.; Refson, K.; Payne, M. C. First Principles Methods Using CASTEP. *Z. Kristallogr. − Cryst. Mater.* **2005**, *220*, 567−570.

(31) Perdew, J. P.; Burke, K.; Ernzerhof, M. Generalized Gradient Approximation Made Simple. *Phys. Rev. Lett.* **1996**, *77*, 3865−3868.

(32) Vanderbilt, D. Soft Self-Consistent Pseudopotentials in a Generalized Eigenvalue Formalism. *Phys. Rev. B* **1990**, *41*, 7892−7895.

(33) Monkhorst, H. J.; Pack, J. D. Special Points for Brillouin-Zone Integrations. *Phys. Rev. B* **1976**, *13*, 5188−5192.

(34) Middlemiss, D. S.; Ilott, A. J.; Clément, R. J.; Strobridge, F. C.; Grey, C. P. Density Functional Theory-Based Bond Pathway Decompositions of Hyperfine Shifts: Equipping Solid-State NMR to Characterize Atomic Environments in Paramagnetic Materials. *Chem. Mater.* **2013**, *25*, 1723−1734.

(35) Mayo, M.; Griffith, K. J.; Pickard, C. J.; Morris, A. J. Ab Initio Study of Phosphorus Anodes for Lithium- and Sodium-Ion Batteries. *Chem. Mater.* **2016**, *28*, 2011−2021.

(36) Morita, R.; Gotoh, K.; Dahbi, M.; Kubota, K.; Komaba, S.; Tokiwa, K.; Arabnejad, S.; Yamashita, K.; Deguchi, K.; Ohki, S.; Shimizu, T.; Laskowski, R.; Ishida, H. States of Thermochemically or Electrochemically Synthesized Na_xP_y Compounds Analyzed by Solid State ^{23}Na and ^{31}P Nuclear Magnetic Resonance with Theoretical Calculation. *J. Power Sources* **2019**, *413*, 418−424.

(37) Zhang, W.; Mao, J.; Li, S.; Chen, Z.; Guo, Z. Phosphorus-Based Alloy Materials for Advanced Potassium-Ion Battery Anode. *J. Am. Chem. Soc.* **2017**, *139*, 3316−3319.

(38) Liu, X. H.; Zhong, L.; Huang, S.; Mao, S. X.; Zhu, T.; Huang, J. Y. Size-Dependent Fracture of Silicon Nanoparticles during Lithiation. *ACS Nano* **2012**, *6*, 1522−1531.

(39) Evans, M. L.; Morris, A. J. Research Data Supporting: Tin Phosphide Anodes for Potassium-Ion Batteries: Insights From Crystal Structure Prediction, https://zenodo.org/record/6546650#.YtVg-i1h1ao (accessed June 30, 2022) DOI: 10.5281/zenodo.6546649.

(40) Bartók, A. P.; Yates, J. R. Regularized SCAN Functional. *J. Chem. Phys.* **2019**, *150*, No. 161101.

(41) Sun, J.; Ruzsinszky, A.; Perdew, J. Strongly Constrained and Appropriately Normed Semilocal Density Functional. *Phys. Rev. Lett.* **2015**, *115*, No. 036402.

(42) Marbella, L. E.; Millstone, J. E. NMR Techniques for Noble Metal Nanoparticles. *Chem. Mater.* **2015**, *27*, 2721−2739.
(43) Protesescu, L.; Rossini, A. J.; Kriegner, D.; Valla, M.; De Kergommeaux, A.; Walter, M.; Kravchyk, K. V.; Nachtegaal, M.; Stangl, J.; Malaman, B.; Reiss, P.; Lesage, A.; Emsley, L.; Copéret, C.; Kovalenko, M. V. Unraveling the Core-Shell Structure of Ligand-Capped Sn/SnO_x Nanoparticles by Surface-Enhanced Nuclear Magnetic Resonance, Mössbauer, and X-Ray Absorption Spectroscopies. *ACS Nano* **2014**, *8*, 2639−2648.
(44) Rees, G. J.; Orr, S. T.; Barrett, L. O.; Fisher, J. M.; Houghton, J.; Spikes, G. H.; Theobald, B. R. C.; Thompsett, D.; Smith, M. E.; Hanna, J. V. Characterisation of Platinum-Based Fuel Cell Catalyst Materials Using ^{195}Pt Wideline Solid State NMR. *Phys. Chem. Chem. Phys.* **2013**, *15*, 17195−17207.
(45) Sheng, T. C.; Kirszensztejn, P.; Bell, T. N.; Gay, I. D. ^{31}P And ^{119}Sn High Resolution Solid State CP/MAS NMR Study of Al_2O_3-SnO_2 Systems. *Catal. Lett.* **1994**, *23*, 119−126.
(46) Marbella, L. E.; Evans, M. L.; Groh, M. F.; Nelson, J.; Griffith, K. J.; Morris, A. J.; Grey, C. P. Sodiation and Desodiation via Helical Phosphorus Intermediates in High-Capacity Anodes for Sodium-Ion Batteries. *J. Am. Chem. Soc.* **2018**, *140*, 7994−8004.
(47) Key, B.; Morcrette, M.; Tarascon, J. M.; Grey, C. P. Pair Distribution Function Analysis and Solid State NMR Studies of Silicon Electrodes for Lithium Ion Batteries: Understanding the (de)Lithiation Mechanisms. *J. Am. Chem. Soc.* **2011**, *133*, 503−512.
(48) Jung, H.; Allan, P. K.; Hu, Y. Y.; Borkiewicz, O. J.; Wang, X. L.; Han, W. Q.; Du, L. S.; Pickard, C. J.; Chupas, P. J.; Chapman, K. W.; Morris, A. J.; Grey, C. P. Elucidation of the Local and Long-Range Structural Changes That Occur in Germanium Anodes in Lithium-Ion Batteries. *Chem. Mater.* **2015**, *27*, 1031−1041.
(49) Stratford, J. M.; Mayo, M.; Allan, P. K.; Pecher, O.; Borkiewicz, O. J.; Wiaderek, K. M.; Chapman, K. W.; Pickard, C. J.; Morris, A. J.; Grey, C. P. Investigating Sodium Storage Mechanisms in Tin Anodes: A Combined Pair Distribution Function Analysis, Density Functional Theory, and Solid-State NMR Approach. *J. Am. Chem. Soc.* **2017**, *139*, 7273−7286.
(50) León, B.; Corredor, J. I.; Tirado, J. L.; Pérez-Vicente, C. On the Mechanism of the Electrochemical Reaction of Tin Phosphide with Lithium. *J. Electrochem. Soc.* **2006**, *153*, A1829.
(51) Mayo, M.; Griffith, K. J.; Pickard, C. J.; Morris, A. J. Ab Initio Study of Phosphorus Anodes for Lithium- and Sodium-Ion Batteries. *Chem. Mater.* **2016**, *28*, 2011−2021.
(52) Frerichs, J. E.; Koppe, J.; Engelbert, S.; Heletta, L.; Brunklaus, G.; Winter, M.; Madsen, G. K. H.; Hansen, M. R. ^{119}Sn and ^{7}Li Solid-State NMR of the Binary Li-Sn Intermetallics: Structural Fingerprinting and Impact on the Isotropic ^{119}Sn Shift via DFT Calculations. *Chem. Mater.* **2021**, *33*, 3499−3514.
(53) Frerichs, J. E.; Ruttert, M.; Böckmann, S.; Winter, M.; Placke, T.; Hansen, M. R. Identification of LixSn Phase Transitions during Lithiation of Tin Nanoparticle-Based Negative Electrodes from Ex Situ ^{119}Sn MAS NMR and Operando ^{7}Li NMR and XRD. *ACS Appl. Energy Mater.* **2021**, *4*, 7278−7287.
(54) Kim, Y.-U.; Lee, C. K.; Sohn, H.-J.; Kang, T. Reaction Mechanism of Tin Phosphide Anode by Mechanochemical Method for Lithium Secondary Batteries. *J. Electrochem. Soc.* **2004**, *151*, A933.
(55) Ueda, A.; Nagao, M.; Inoue, A.; Hayashi, A.; Seino, Y.; Ota, T.; Tatsumisago, M. Electrochemical Performance of All-Solid-State Lithium Batteries with Sn_4P_3 Negative Electrode. *J. Power Sources* **2013**, *244*, 597−600.
(56) Ding, Y.; Li, Z. F.; Timofeeva, E. V.; Segre, C. U. In Situ EXAFS-Derived Mechanism of Highly Reversible Tin Phosphide/Graphite Composite Anode for Li-Ion Batteries. *Adv. Energy Mater.* **2018**, *8*, No. 1702134.
(57) Kim, Y.; Kim, Y.; Choi, A.; Woo, S.; Mok, D.; Choi, N. S.; Jung, Y. S.; Ryu, J. H.; Oh, S. M.; Lee, K. T. Tin Phosphide as a Promising Anode Material for Na-Ion Batteries. *Adv. Mater.* **2014**, *26*, 4139−4144.
(58) Qian, J.; Xiong, Y.; Cao, Y.; Ai, X.; Yang, H. Synergistic Na-Storage Reactions in Sn_4P_3 as a High-Capacity, Cycle-Stable Anode of Na-Ion Batteries. *Nano Lett.* **2014**, *14*, 1865−1869.
(59) Sultana, I.; Ramireddy, T.; Rahman, M. M.; Chen, Y.; Glushenkov, A. M. Tin-Based Composite Anodes for Potassium-Ion Batteries. *Chem. Commun.* **2016**, *52*, 9279−9282.
(60) Kropf, A. J.; Tostmann, H.; Johnson, C. S.; Vaughey, J. T.; Thackeray, M. M. An in Situ X-Ray Absorption Spectroscopy Study of InSb Electrodes in Lithium Batteries. *Electrochem. Commun.* **2001**, *3*, 244−251.
(61) Fransson, L. M. L.; Vaughey, J. T.; Benedek, R.; Edström, K.; Thomas, J. O.; Thackeray, M. M. Phase Transitions in Lithiated Cu2Sb Anodes for Lithium Batteries: An in Situ X-Ray Diffraction Study. *Electrochem. Commun.* **2001**, *3*, 317−323.
(62) Li, H.; Huang, X.; Chen, L.; Wu, Z.; Liang, Y. High Capacity Nano-Si Composite Anode Material for Lithium Rechargeable Batteries. *Electrochem. Solid-State Lett.* **1999**, *2*, 547−549.
(63) Khomenko, V. G.; Barsukov, V. Z.; Doninger, J. E.; Barsukov, I. V. Lithium-Ion Batteries Based on Carbon-Silicon-Graphite Composite Anodes. *J. Power Sources* **2007**, *165*, 598−608.
(64) Magasinski, A.; Dixon, P.; Hertzberg, B.; Kvit, A.; Ayala, J.; Yushin, G. High-Performance Lithium-Ion Anodes Using a Hierarchical Bottom-up Approach. *Nat. Mater.* **2010**, *9*, 353−358.

NOTE ADDED IN PROOF

NMR data may be found on the Open Science Framework at https://osf.io/xmcs5/. Computational data for K−Sn−P phase prediction may be found at https://doi.org/10.5281/zenodo.6546649.

https://doi.org/10.1021/acs.chemmater.2c01570
Chem. Mater. XXXX, XXX, XXX−XXX